Nanoanalytical analysis of bisphosphonate-driven alterations of microcalcifications using a 3D hydrogel system and in vivo mouse model

Jessica L. Ruiz[a,b] , Joshua D. Hutcheson[c] , Luis Cardoso[d] , Amirala Bakhshian Nik[c] ,
Alexandra Condado de Abreu[e] , Tan Pham[a] , Fabrizio Buffolo[a] , Sara Busatto[f,g] , Stefania Federici[h] ,
Andrea Ridolfi[i,j,k] , Masanori Aikawa[a,l] , Sergio Bertazzo[e] , Paolo Bergese[g,i,m] , Sheldon Weinbaum[d,1] ,
and Elena Aikawa[a,l,1]

[a]Center for Interdisciplinary Cardiovascular Sciences, Cardiovascular Medicine, Brigham and Women's Hospital, Harvard Medical School, Boston, MA 02115; [b]Department of Pediatrics, Boston Children's Hospital, Harvard Medical School, Boston, MA 02115; [c]Department of Biomedical Engineering, Florida International University, Miami, FL 33174; [d]Department of Biomedical Engineering, City College of New York, New York, NY 10031; [e]Department of Medical Physics and Biomedical Engineering, University College London, WC1E 6BT London, United Kingdom; [f]Vascular Biology Program, Boston Children's Hospital, Harvard Medical School, Boston, MA 02115; [g]Department of Molecular and Translational Medicine, University of Brescia, 25123 Brescia, Italy; [h]Department of Mechanical and Industrial Engineering, National Interuniversity Consortium of Materials Science and Technology, University of Brescia, 25123 Brescia, Italy; [i]Consorzio Interuniversitario per lo Sviluppo dei Sistemi a Grande Interfase, 50019 Florence, Italy; [j]National Research Council, Institute of Nanostructured Materials, 40129 Bologna, Italy; [k]Department of Chemistry, University of Florence, 50019 Florence, Italy; [l]Center for Excellence in Vascular Biology, Cardiovascular Medicine, Brigham and Women's Hospital, Harvard Medical School, Boston, MA 02115; and [m]Institute for Research and Biomedical Innovation, National Research Council, 90146 Palermo, Italy

Vascular calcification predicts atherosclerotic plaque rupture and cardiovascular events. Retrospective studies of women taking bisphosphonates (BiPs), a proposed therapy for vascular calcification, showed that BiPs paradoxically increased morbidity in patients with prior acute cardiovascular events but decreased mortality in event-free patients. Calcifying extracellular vesicles (EVs), released by cells within atherosclerotic plaques, aggregate and nucleate calcification. We hypothesized that BiPs block EV aggregation and modify existing mineral growth, potentially altering microcalcification morphology and the risk of plaque rupture. Three-dimensional (3D) collagen hydrogels incubated with calcifying EVs were used to mimic fibrous cap calcification in vitro, while an ApoE$^{-/-}$ mouse was used as a model of atherosclerosis in vivo. EV aggregation and formation of stress-inducing microcalcifications was imaged via scanning electron microscopy (SEM) and atomic force microscopy (AFM). In both models, BiP (ibandronate) treatment resulted in time-dependent changes in microcalcification size and mineral morphology, dependent on whether BiP treatment was initiated before or after the expected onset of microcalcification formation. Following BiP treatment at any time, microcalcifications formed in vitro were predicted to have an associated threefold decrease in fibrous cap tensile stress compared to untreated controls, estimated using finite element analysis (FEA). These findings support our hypothesis that BiPs alter EV-driven calcification. The study also confirmed that our 3D hydrogel is a viable platform to study EV-mediated mineral nucleation and evaluate potential therapies for cardiovascular calcification.

atherosclerosis | microcalcification | bisphosphonate | extracellular vesicles

Atherosclerotic plaque rupture is the leading cause of myocardial infarction and stroke (1, 2). Studies assessing the correlation between calcium scores and cardiovascular events have demonstrated a predictive power that is superior to and independent from that of lipid scores (3, 4). Additionally, clinical imaging studies have revealed that the risk of plaque rupture is further heightened by the presence of small, "spotty" calcifications, or microcalcifications (5, 6), and cardiovascular risk is inversely correlated with the size of calcific deposits, quantified as a calcium density score (7). Indeed, computational modeling has demonstrated that, while large calcifications can reinforce the fibrous cap (8), microcalcifications (typically 5 to 15 μm in diameter) uniquely mediate an increase in mechanical stress of the relatively soft, collagen-rich fibrous cap (9–12).

Histologic studies have revealed the presence of cell-derived vesicles within calcifying atherosclerotic lesions (13–16). The inflammatory environment of the atherosclerotic lesion can induce vascular smooth muscle cells (vSMCs) to take on an osteochondrogenic phenotype and release calcifying extracellular vesicles (EVs) (17–19). Macrophages have also been shown to release procalcifying vesicles (20, 21). Thus, just as bone formation is hypothesized to be an active, cell-driven process (22, 23), mediated by calcifying matrix vesicles, atheroma-associated calcification may similarly be initiated by the production and aggregation of calcifying EVs (11, 20, 24–28).

Significance

The most common cause of heart attacks or strokes is the rupture of thin fibrous caps that cover vulnerable plaques within blood vessels. Small mineral deposits, called microcalcifications, increase local tissue stress and thereby increase the risk of cap rupture. We report here the use of a three-dimensional collagen hydrogel model of fibrous cap calcification and a complementary mouse model of plaque formation to determine whether bisphosphonate (BiP) therapy, commonly used to treat bone loss, alters microcalcification formation. The results showed that BiP treatment resulted in time-dependent changes in microcalcification size and mineral morphology, dependent on whether BiP treatment was initiated before or after the expected onset of microcalcification formation.

One proposed strategy for halting pathologic calcification has been the use of bisphosphonates (BiPs). BiPs are analogs of pyrophosphate (29), a naturally occurring compound derived in vivo from adenosine triphosphate (ATP) (30). Pyrophosphate binds to calcium phosphate and inhibits calcification via physicochemical mechanisms, namely, by blocking calcium and phosphate ions from forming crystals, preventing crystal aggregation, and preventing mineral transformation from amorphous calcium phosphate to hydroxyapatite (29). BiPs were identified as pyrophosphate analogs that, unlike pyrophosphate itself, resist enzymatic hydrolysis. A second, distinct property of BiPs is the ability to inhibit bone resorption via biological activity directed against osteoclasts following osteoclast endocytosis of the BiP molecule adsorbed to the surface of bone (29, 31). First-generation, or nonnitrogen-containing BiPs, are incorporated into nonhydrolyzable ATP analogs, and induce osteoclast apoptosis by limiting ATP-dependent enzymes. In contrast, nitrogen-containing BiPs inhibit farnesyl pyrophosphate synthetase and thereby induce osteoclast apoptosis (31).

In vivo animal investigations have been performed to explore the potential for BiPs to inhibit cardiovascular calcification. Studies of first-generation BiPs revealed that the doses required to inhibit cardiovascular calcification also critically compromised normal bone mineralization (29, 32). However, newer, nitrogen-containing BiPs effectively arrested cardiovascular calcification in animal models at doses that did not compromise bone formation (32). Further, while it has been proposed that BiP treatment modifies cardiovascular calcification via its impact on bone-regulated circulating calcium and phosphate levels, a study in uremic rats demonstrated that BiP treatment inhibited medial aortic calcification with no significant change in plasma calcium and phosphate levels (33). The same study demonstrated that BiP treatment inhibited calcification of explanted rat aortas, indicating that BiPs can act directly on vascular tissue, independent of bone metabolism (33).

Retrospective clinical data examining the effect of BiP therapy on cardiovascular calcification has demonstrated conflicting findings and intriguing paradoxes. In women with chronic kidney disease, BiP therapy decreased the mortality rate for patients without a prior history of cardiovascular disease (34), but for those patients with a history of prior cardiovascular events, BiP therapy was associated with an increased mortality rate (35). In another study, BiP therapy correlated with a lower rate of cardiovascular calcification in older patients (>65 y), but a greater rate in younger patients (<65 y) (36). These clinical findings motivated our study, in which we sought to further understand how BiP therapy impacts cardiovascular outcomes. Given that cardiovascular calcification, and especially the presence of microcalcification, is a strong and independent risk factor for adverse cardiac events, and BiPs are prescribed to modulate pathologies of mineralization, we hypothesize that BiPs modulate cardiovascular outcomes by altering the dynamics of cardiovascular calcification.

EVs are smaller than the resolution limits of traditional microscopy techniques, hindering studies into the mechanisms of calcification nucleation and growth. We previously developed an in vitro collagen hydrogel platform that allowed the visualization of calcific mineral development mediated by EVs isolated from vSMCs (24). Using superresolution microscopy, confocal, and electron microscopy techniques, we showed that calcification requires the accumulation of EVs that aggregate and merge to build mineral. Collagen serves as a scaffold that promotes associations between EVs that spread into interfibrillar spaces. The resultant mineral that forms within the collagen hydrogel appears spectroscopically similar to microcalcifications in human tissues and allows the study of these structures on the time scale of 1 wk. In this study, we utilized this three-dimensional (3D) acellular platform to examine the direct effect of ibandronate, a nitrogen-containing BiP, on the EV-directed nucleation and growth of microcalcifications, a process that cannot be isolated from cellular and tissue-level mechanisms in a more complex,

in vivo system. In parallel, we utilized a mouse model of atherosclerosis to assess the effect of ibandronate therapy on plaque-associated calcification, comparing mineral morphologies between the in vitro and in vivo samples. We hypothesize that BiPs block EV aggregation and modify existing mineral growth, potentially altering microcalcification morphology and the risk of plaque rupture. Understanding the EV-specific action of BiPs is imperative both to develop anticalcific therapeutics targeting EV mineralization and to understand one potential mechanism driving the cardiovascular impact of BiPs used in clinical settings.

Results

The 3D collagen hydrogels were incubated with calcifying EVs in osteogenic medium for 8 d (Fig. 1). The characterization of calcifying EVs is presented in the supplemental information (*SI Appendix*, Figs. S1–S3). Scanning electron microscopy (SEM) revealed the aggregation of EVs along and between collagen fibrils (Fig. 2 *A*, *B*, and *D*). The EV aggregates formed in vitro resembled aggregates of dense, spherical particles visualized within a calcified region of a human atherosclerotic plaque, imaged using density-dependent color SEM (DDC-SEM) (37) (Fig. 2*C*). Using transmission electron microscopy (TEM), similar, rough appearing vesicular structures were identified in sections of EV-incubated hydrogels and in human atherosclerotic tissue (Fig. 2 *E* and *F*, respectively). Confocal microscopy of collagen hydrogels stained with a fluorescent calcium tracer confirmed that incubation with calcifying EVs led to the formation of structures composed of calcium phosphate mineral, i.e., microcalcifications (Fig. 3*A*). Energy dispersive spectroscopy (EDS), a technique used to analyze elemental composition concurrent with SEM, demonstrated that EV aggregates formed in our 3D platform contained phosphorous and calcium (Fig. 3*B*). EDS mapping of EV aggregates (Fig. 3*C*) further visualized the phosphorous (Fig. 3*D*) and calcium (Fig. 3*E*) content of these structures. Additionally, multiscale finite element analysis (FEA) predicted a 350% increase in tissue stress (stress concentration factor [SCF]) that would be associated with a representative microcalcification formed in our in vitro 3D platform (*SI Appendix*, Fig. S4).

To investigate the effect of BiP treatment on the formation and growth of EV-nucleated microcalcifications, a single dose of the BiP ibandronate was added simultaneously with calcifying EVs to the 3D collagen platform on day 0 of incubation. After 8 d of incubation, SEM images demonstrated that, compared to untreated samples (Fig. 4 *A* and *C*), BiP treatment on day 0 reduced the maximum size of microcalcifications formed in the 3D system (Fig. 4 *B* and *D*). A custom image analysis algorithm was used to analyze a representative sample of high-powered fields from each group and revealed a statistically significant decrease in maximum microcalcification size in BiP-treated samples (Fig. 4*E*). EDS analysis of a representative sample for each group further indicated that BiP treatment altered the elemental composition of microcalcifications, with a significant decrease in both calcium and phosphorous (Fig. 4*F*). There was no difference in tissue non-specific alkaline phosphatase (ALP) activity
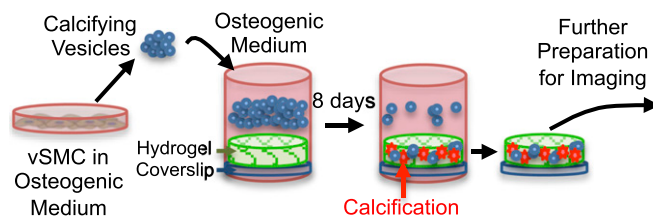

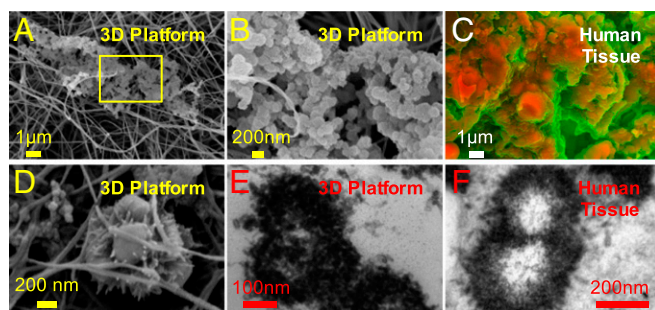**Fig. 1.** Schematic of assembly and use of 3D collagen platform.

Fig. 2. The 3D collagen-EV platform recapitulated microcalcifications seen in human atheroma. (*A*) SEM image of a microcalcification formed in the 3D collagen platform after 8 d of incubation with calcifying EVs. (*B*) Higher magnification view of yellow-outlined region in *B*. (*C*) DDC-SEM image of calcified atherosclerotic plaque from a human carotid endarterectomy sample. (*D*) Higher magnification SEM image of EVs aggregating in the 3D collagen platform. (*E*) TEM image of a microcalcification formed in the 3D collagen platform. (*F*) TEM image of calcified atherosclerotic plaque from human tissue sample.

between BiP-treated and untreated EVs following up to 4 h of incubation (*SI Appendix*, Fig. S5).

Next, we examined the time-dependent effect of BiP treatment on in vitro microcalcification formation (Fig. 5*A*). Each sample received a single dose of BiP, but the time at which the BiP was added varied. Quantified using a fluorescent-based assay, the amount of calcific mineral detected on day 8 significantly varied across treatment groups (Fig. 5*B*, $P = 0.0025$, via one-way repeated measures ANOVA). Multiple comparisons testing revealed a significant difference between the untreated control and samples treated on day 6 (adjusted $P = 0.027$), but no difference between the control and samples treated with single-dose BiP on days 0, 2, or 4 (Fig. 5*B*). Notably, a control experiment demonstrated that the degree of calcification observed was significantly higher for all treatment groups if EVs were incubated in osteogenic medium, as compared to normal medium (*SI Appendix*, Fig. S6).

Fourier-transform infrared spectroscopy (FTIR) analysis of all treatment groups revealed prominent peaks in the 900 to 1,200 cm^{-1} region, associated with the stretching modes of the P-O bond in phosphate (38, 39) (Fig. 5*C*). In the control group, there was a predominant peak at 1,027 cm^{-1}, with a prominent shoulder at 1,100 cm^{-1} and a small shoulder at 960 cm^{-1}, consistent with the known spectral features of hydroxyapatite (38–44). With BiP treatment, the shoulders at 1,100 cm^{-1} and 960 cm^{-1} generally became less prominent, and the predominant P-O peak decreases in frequency to around 1,021 cm^{-1} for the samples treated on day 2 and day 6, and 1,017 cm^{-1} for the sample treated on day 4 (Fig. 5*C*). Given that it has been previously shown that spectral features sharpen with mineral maturity and crystallinity (39, 42, 43), it is possible that BiP treatment resulted in the formation of a less mature mineral. Additionally, the predominant P-O peak decreased in frequency from 1,027 cm^{-1} to around 1,021 cm^{-1} in the day 2 and day 6 samples, and 1,017 cm^{-1} in the day 4 sample. It has been suggested that a decrease in the frequency of this peak is seen in less crystalline apatite (39). It has also been shown that the ratio of 1,030 cm^{-1} to 1,020 cm^{-1} peak intensities are associated with mineral crystallinity, and thereby, maturity (42, 44). Thus, it is possible that the decreased frequency of this peak occurred due to the presence of a less crystalline and less mature mineral in the BiP-treated samples. The FTIR spectra did not demonstrate any direct evidence of BiP incorporation into the mineral formed, but this was likely due to the P-O bonds of the

bisphosphonate overlapping with the P-O bonds of the hydroxyapatite formed. The FTIR spectra for all groups demonstrated the presence of carbonate substitution into the mineral, as evidenced by peak at 873 cm^{-1}, which represents C-O bond bending, and the peak at 1,420 cm^{-1}, which represents C-O stretching (39–42, 44–46) (Fig. 5*C*). The peak at 873 cm^{-1} has been suggested to be associated with type B carbonate, that is, carbonate groups substituted for phosphate groups within hydroxyapatite (45). Finally, the peak seen at 1,650 to 1,655 cm^{-1} (Fig. 5*C*) has been associated with the amide I band of protein, specifically C = O peptide double bond (41, 42, 44).

Atomic force microscopy based force spectroscopy (AFM-FS) provided a comparison of the properties of our samples by probing the forces experienced by the AFM tip when indenting the sample (*SI Appendix*, Fig. S7). In this case, we measured the tip-sample normalized detachment force (NDF), which represents the force needed by the AFM tip to snap free from the sample. NDF was normalized by the detachment force from the free solid substrate (mica) and used to characterize the mechanical properties and in turn composition and structure of the samples. The NDF of the isolated EVs (*SI Appendix*, Fig. S7, red bar) resulted significantly higher than that of the mineral (*SI Appendix*, Fig. S7, green bar). This is intuitive and reasonable in first approximation, given that a lower force is needed to detach the tip from the hard mineral with respect to that needed to detach it from the sticky lipid bilayer of the EVs. We found that all five experimental groups (*SI Appendix*, Fig. S7, blue bars) have a NDF which falls in between the values obtained for the native EVs and the pure mineral. This characteristic intermediate physicochemical interaction with the AFM tip suggests that the EV-nucleated microcalcifications are made of a "composite material" of EVs and calcium phosphate mineral.

SEM and AFM imaging revealed that BiP treatment altered microcalcification morphology in a time-dependent manner (Fig. 6). While untreated microcalcifications were more dense-appearing, elongated structures (Fig. 6*A*), BiP-treated microcalcifications varied in their morphology depending on the timing of BiP treatment. Microcalcifications from samples that underwent early (day 2) BiP treatment had a significantly more circular morphology compared to all other groups (Fig. 6 *B* and *I*), with a ∼50% reduction in height measured by AFM (Fig. 6*F*). In samples that underwent treatment on day 4, the resulting microcalcifications had no significant difference in shape, size, or height (Fig. 6 *C, G, I,* and *J*). Samples treated on day 2 or day 4
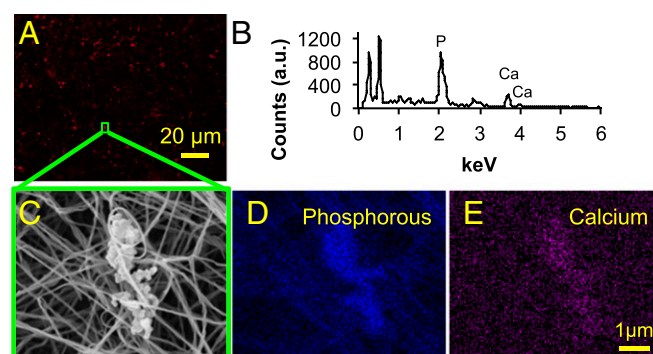
Fig. 3. The 3D collagen-EV platform mediated the deposition of calcium phosphate mineral. (*A*) Collagen hydrogel following 8 d of incubation with calcifying EVs, stained with a near-infrared fluorescent calcium tracer, and imaged using confocal microscopy. (*B*) Representative EDS spectrum of a microcalcification in the 3D collagen platform. (*C*) Microcalcification imaged in the 3D collagen platform using SEM. EDS was conducted for this microcalcification, yielding elemental maps of phosphorous (*D*) and calcium (*E*).

Ruiz et al.
Nanoanalytical analysis of bisphosphonate-driven alterations of microcalcifications using a 3D hydrogel system and in vivo mouse model

PNAS | 3 of 10
https://doi.org/10.1073/pnas.1811725118

CELL BIOLOGY

had a more fine-textured mineral structure compared to other groups (Fig. 6 *B* and *C*). Following treatment on day 6, the final microcalcifications observed were of a less circular, more elongated morphology akin to untreated controls (Fig. 6 *A*, *D*, and *I*). While these microcalcifications were of a significantly larger area compared to all other groups (Fig. 6*J*), their height measured by AFM was reduced by ∼80% (Fig. 6*H*), and they visually appeared to be composed of some areas of rough mineral aggregates and others of thin, sheet-like regions interrupted by several gaps (Fig. 6*D*). Finally, FEA revealed a significant, threefold reduction in the SCF predicted for microcalcifications formed following single-dose BiP treatment at any time, versus those from the control group (Fig. 7).

A mouse model of atherosclerosis was used to assess the effect of BiP treatment on plaque-associated calcification in vivo. ApoE$^{-/-}$ mice were fed an atherogenic diet and started on twice weekly BiP treatment (ibandronate, 2 mg/kg per dose) (Fig. 8*A*) at different stages of vascular calcification based on prior studies of the time course of the onset of microcalcification formation (18, 24, 47–49). Specifically, BiP was given after 5 wk of diet, before the expected onset of microcalcification ("week 5 BiP") (48), after 10 wk of diet, at the expected time of initial microcalcification formation ("week 10 BiP") (18, 24), or after 15 wk of diet, once microcalcification formation has been established ("week 15 BiP") (18, 24, 47–49), further detailed in *SI Appendix*. Density-dependent color SEM (DDC-SEM) (37) images were obtained of atherosclerotic plaque-associated calcification in the aortic root of these mice following 25 wk of diet (representative histological images demonstrating atherosclerosis and calcification in these lesions are provided in *SI Appendix*, Figs. S8 and S9). The images obtained from this mouse model visualized vascular calcification at a more advanced stage in which multiple microcalcifications aggregate together into larger calcification areas (Fig. 8), complementary to the images of individual microcalcifications visualized using our in vitro acellular platform (Fig. 6).

In control mice, the areas of microcalcification (orange) were more confluent with a larger average area per microcalcification (Fig. 8 *B* and *D*), with a high degree of quantified surface roughness (Fig. 8*C*). In the mice given BiP treatment prior to the onset of calcification (week 5 of diet), the areas of microcalcification had a similar degree of quantified surface roughness compared to the control group (Fig. 8*C*), but the average area per microcalcification was smaller (Fig. 8 *B* and *E*). Compared to the control and week 5 groups, the microcalcifications visualized in the week 10 and week 15 groups were more loosely aggregated together and of a significantly smaller average area (Fig. 8 *B*, *F*, and *G*). In mice treated with BiP starting at the onset of calcification formation (week 10 of diet), the imaged mineral had the lowest degree of surface roughness (Fig. 8 *C* and *F*). In comparison, mice started on BiP treatment once calcification formation had been established (week 15 of diet) had mineral that was of a moderate degree of surface roughness (Fig. 8 *C* and *G*). Thus, BiP treatment was associated with changes in the morphology of microcalcifications as they aggregated together in vivo, just as we observed changes in individual microcalcification morphology following BiP treatment via the in vitro acellular platform (Fig. 6 *A*–*D*, *I*, *J* vs. Fig. 8 *B*–*G*).

Discussion

This study was motivated by observed differences in cardiovascular outcomes among patients who started taking BiPs at different ages or different stages of cardiovascular disease (34–36). Given that cardiovascular calcification, and especially the presence of microcalcifications, is a strong and independent risk factor for adverse cardiac events, and BiPs are prescribed to treat

pathologies of mineralization, we hypothesized that one role of BiPs in modulating cardiovascular outcomes was by altering the dynamics of EV-mediated microcalcification formation.

Using a 3D, acellular platform, our study unveiled a direct, physicochemical interaction between the BiP ibandronate and EV-nucleated microcalcifications. Our findings demonstrated that early (day 0 and day 2) BiP treatment of calcifying EVs resulted in smaller, more circular microcalcifications with a more fine-textured mineral structure and no significant difference in the total amount of mineral formed, compared to the control. In contrast, samples that underwent later BiP treatment on day 6 of incubation produced microcalcifications of a significantly larger size with a rough and interrupted mineral structure, and a significantly greater amount of mineral measured overall compared to all other groups, including the untreated control. These findings were complemented by changes in calcific mineral morphology in an in vivo mouse model of atherosclerosis, in which vascular calcification was captured at a more advanced stage of aggregation within atherosclerotic lesions. While untreated mice and mice started early (week 5 of diet) on BiP treatment demonstrated plaque-associated calcification with a high degree of surface roughness, later treatment (weeks 10 and 15 of diet) resulted in mineral with a lower degree of roughness, and all BiP-treated groups (weeks 5, 10, and 15 of diet) had a smaller average area per individual microcalcification as compared to the control.
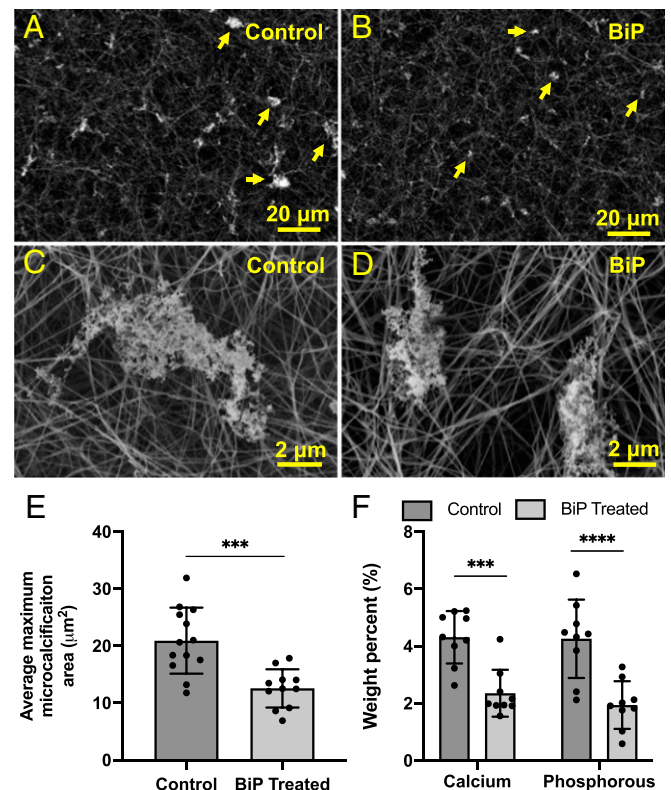
Fig. 4. BiP reduced the maximum size of calcific EV aggregates visualized via SEM. Changes in microcalcification size can be seen at low magnification (*A* vs. *B*) and high magnification (*C* vs. *D*). The average cross-sectional area of the five largest microcalcifications per high-powered field was significantly lower in the BiP-treated group versus the control group (*E*, n = 3 biological replicates). Elemental calcium and phosphorous composition of control and BiP-treated microcalcifications measured via EDS (*F*, nine technical replicates per group, n = 1 biological replicates, ***P < 0.001, ****P < 0.0001, error bars represent SD).

Fig. 5. The formation of microcalcifications varied significantly with single-dose BiP treatment in a time-dependent manner. Schematic depicting the experimental setup for treating samples with a single dose of BiP at different times (*A*). The a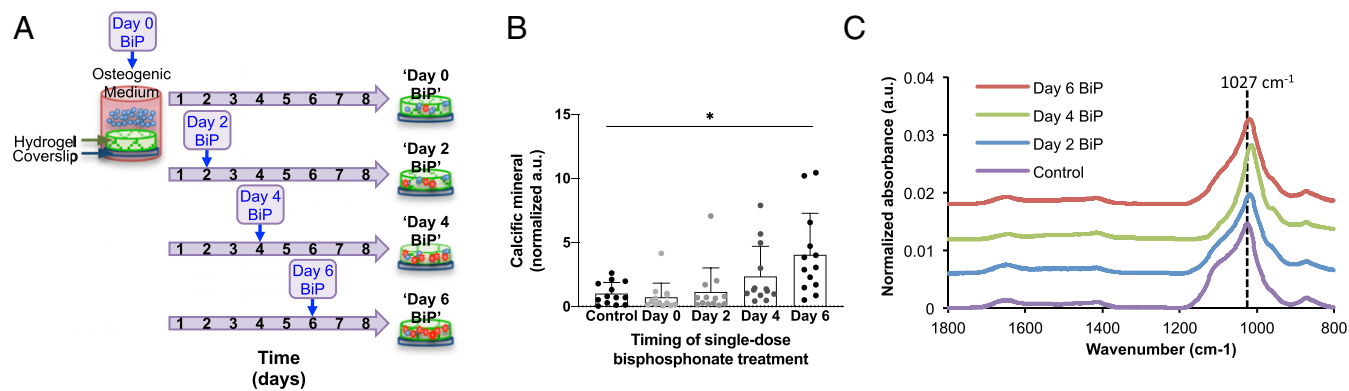mount of calcium phosphate mineral formed in each sample was measured using a fluorescent-based assay and varied significantly across treatment groups (*B*, $P = 0.0025$ via one-way ANOVA; $n = 5$ biological replicates), with a significant difference between control and day 6 groups (*$P = 0.027$, error bars represent SD). The chemical composition of microcalcifications formed in each sample was measured using FTIR, with a representative spectrum shown for each group (*C*).

EV-driven mineral formation in vitro begins after 3 d of incubation in osteogenic medium (24). Thus, treatment with BiP within the first 3 d of incubation leads to microcalcification formation in the presence of BiP molecules, whereas treatment at later time points introduces the influence of BiP to microcalcifications that have already started to form. BiPs are analogous to pyrophosphate, a natural inhibitor of mineral formation that acts to block calcium and phosphate ions from forming crystals, inhibit crystal aggregation, and limit mineral transformation from amorphous calcium phosphate to hydroxyapatite (29). Our findings demonstrated that early BiP treatment resulted in the formation of smaller, circular, less crystalline but more numerous microcalcifications, which may be attributable to the pyrophosphate-like activity of BiP limiting more expansive aggregation and mineralization of calcifying EVs. BiP adsorption onto mineral crystals may further alter crystal growth, size, aggregation, and integrity (50, 51), leading to the observed changes. We further expected a reduction in mineral formation under the influence of BiP, but the overall amount of mineral was unchanged following early BiP treatment. This implies that the main effect of BiP on EV-mediated mineralization is not an antimineralization effect, but rather that BiP influence the morphology and maturity of mineral formed. In addition, it is possible that the concentration of BiP was too low to inhibit mineral formation entirely, and future studies should further explore the effect of different BiP concentrations on EV-mediated microcalcification formation.

In contrast, treatment with BiP on day 6 of incubation resulted in microcalcifications that were larger but thinner, with interruptions to their internal structure. Further, in the acellular system there was a greater total amount of mineral formed in this day 6 group, though the mineral was less crystalline compared to untreated samples. If the effect of later treatment with BiP solely mimicked pyrophosphate, overall we would expect to observe microcalcifications of smaller or equal size to those formed in the absence of BiP, and a reduced or equal amount of mineral measured on day 8. BiP molecules adsorb onto the hydrated surface layer of calcium phosphate mineral (51). In our system, this interaction may have resulted in an alteration of surface chemistry, and this combined with the greater surface area of microcalcifications formed may have led to an increase in mineral detected by the binding assay. However, the mechanism by which the later addition of BiP to already forming microcalcifications led to the formation of larger, thinner, interrupted microcalcifications is unknown and merits further investigation.

Our in vivo findings captured the effect of BiP on vascular calcification at a later stage of the mineralization process, in which individual microcalcifications aggregate together to form larger calcification areas. Initiating BiP treatment at any time, either before (week 5 of diet), at the onset (week 10 of diet), or after (week 15 of diet) of microcalcification formation, decreased the degree to which nascent microcalcifications aggregated together into larger microcalcifications, as quantified by the reduction in the area of the microcalcifications analyzed. Further, later BiP treatment decreased the surface roughness of the mineral that formed. Our in vivo findings complemented our in vitro findings, namely, that BiP changed the morphology of mineral formed. These in vivo changes to larger mineral structures may be attributable to the pyrophosphate-like activity of BiP as it adsorbs onto calcifying EVs and microcalcifications as they form and grow, altering not only the morphology of individual microcalcifications, but also the manner by which microcalcifications aggregate together to form larger calcified structures.

Through imaging analyses, assessment of chemical composition, and FEA, we confirmed that microcalcifications formed in our 3D platform recapitulated human atheroma-associated microcalcifications in morphology and composition and were predicted to cause a notable increase in fibrous cap tensile stress. Only a subset of plaque-associated microcalcifications have high-risk features associated with plaque rupture (9), which are related to size, morphology, alignment within the fibrous cap, and spatial relation to other microcalcifications (9, 10, 52). Therefore, the ability to recapitulate plaque-destabilizing microcalcifications is of particular clinical interest.

This study demonstrated that treatment with BiP at any time point significantly decreased the predicted fibrous cap tensile stress attributable to microcalcifications formed using the 3D platform, despite variation in microcalcification size and morphology among these BiP-treated groups. Importantly, our findings further suggest that BiP treatment mediated changes in mineral morphology in vivo, in a time-dependent manner. Additional in vivo studies are needed to assess the biomechanical and physiologic consequences of these in vivo morphologic changes as they relate to the risk of plaque rupture and adverse cardiac outcomes.

Analysis of the FTIR spectra of untreated and BiP-treated samples revealed that in all conditions, the mineral formed was carbonated hydroxyapatite. Spectral analysis of BiP-treated samples suggested that the mineral formed was likely less mature and less crystalline than untreated controls. Future studies should further
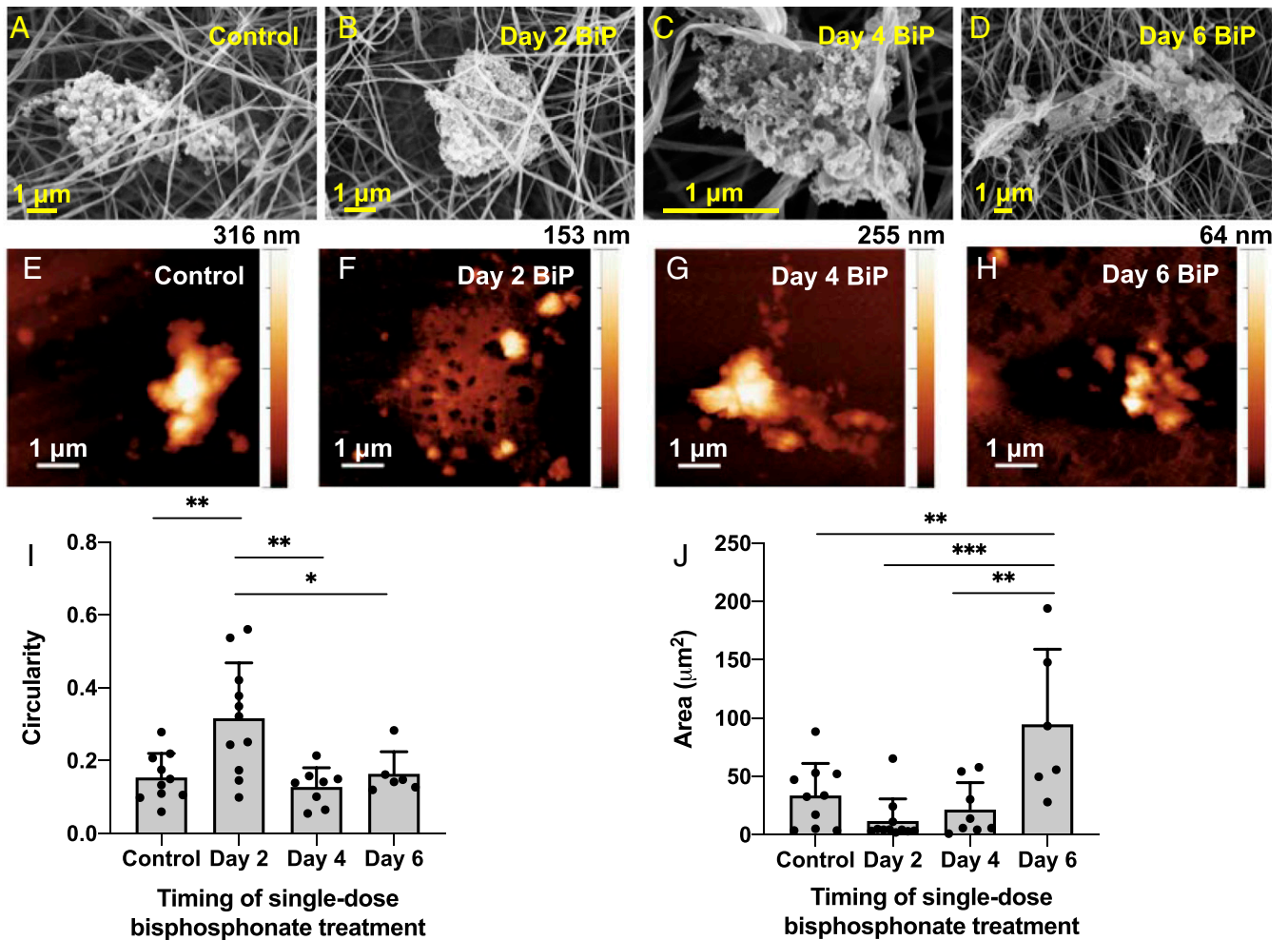
Ruiz et al.
Nanoanalytical analysis of bisphosphonate-driven alterations of microcalcifications using a
3D hydrogel system and in vivo mouse model

PNAS | 5 of 10
https://doi.org/10.1073/pnas.1811725118

Fig. 6. BiP treatment altered microcalcification morphology in a time-dependent manner. SEM (*A–D*) and AFM (*E–H*) were used to image microcalcifications formed in 3D collagen hydrogels that were treated at different times with a single dose of BiP. Microcalcification circularity (*I*) and size (*J*) significantly varied across time points ($n = 4$ biological replicates for control, day 2, day 4 groups, $n = 2$ biological replicates for day 6 group; $*P < 0.05$, $**P < 0.01$, $***P < 0.001$, error bars represent SD).

investigate the composition and crystallinity of EV-derived mineral with and without BiP treatment, both using more advanced FTIR spectral analysis techniques, as well as complementary methods such as Raman spectroscopy and direct measures of crystallinity. Additionally, the FTIR analysis did not reveal any direct evidence of BiP incorporation into the mineral formed, but this was likely secondary to the P-O bonds of the bisphosphonate blending in with the P-O bonds of the hydroxyapatite formed. Future studies using bisphosphonates with more distinct chemical structures should be used to allow for the detection of bisphosphonates using FTIR.

We did not observe any collagen fibril mineralization or other collagen changes in any of our treatment conditions. However, we did visualize that EVs had an affinity for collagen fibrils and used these fibrils as scaffolding as the EVs aggregate and mineralize. We recently showed that calcifying EVs contain annexin A1, which functioned as a membrane-binding protein that mediated EV aggregation (28). Other annexins were also implicated in interactions with collagen in the extracellular matrix and have been hypothesized to mediate calcium influx into EVs (11, 26, 28, 53). Future studies should leverage our 3D platform to study EV-collagen interactions and how BiP may modify said interactions.

Future investigations are also needed to examine the impact of BiP on the cells that produce EVs (e.g., vSMCs and macrophages), and if the calcification potential of EVs is altered by exposure of the parent cells to BiP, particularly in light of the known osteoclast-mediated effects of BiP on bone turnover (31). Additionally, our findings were limited to the consequences of ibandronate treatment, and additional explorations are needed to characterize the effects of different BiPs on microcalcification formation, noting which effects are shared and which are BiP specific.

Furthermore, it remains to be determined if paradoxical cardiovascular outcomes following BiP treatment are, at least in part, a downstream consequence of the impact of BiP treatment on bone metabolism. Additional studies are required to tease apart the relative contributions of physicochemical mechanisms and cellular mechanisms at the level of vascular tissue versus altered circulating factors downstream of bone metabolism, as they relate to vascular calcification. While future studies are needed to examine the impact of BiP on vascular microcalcification formation and adverse cardiac outcomes in vivo in both animal and human studies, our findings provide evidence that differences observed in vivo could be the result, at least in part, from an effect of BiP on EV mineralization directly, a process that cannot be isolated in a more complex, in vivo system.
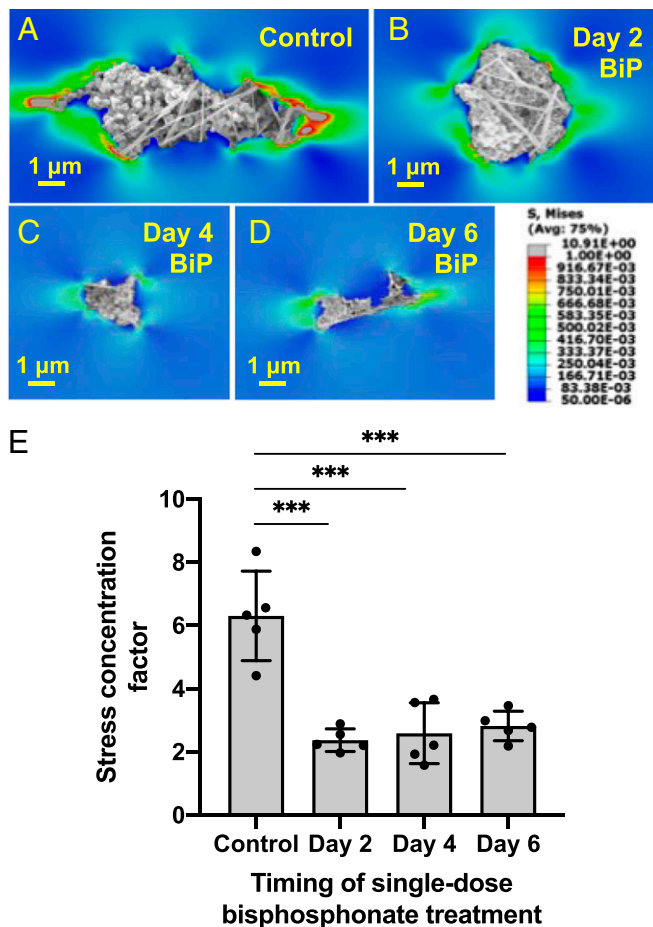
Fig. 7. BiP treatment altered the predicted fibrous cap tensile stress attributed to single microcalcifications, in a time-dependent manner. *A–D* demonstrate FEA analysis of representative microcalcifications treated with BiP at different time points. *E* quantifies the average stress concentration factor for five representative microcalcifications from each BiP-treated group, as compared to untreated microcalcifications (control), ($n = 3$ biological replicates per group, except day 6 group, which reflects $n = 2$ biological replicates, error bars represent SD, ***$P < 0.0001$).

Calcification plays a key role in determining the stability of an atherosclerotic plaque. Pathologic calcification is an active but disordered process that produces one or more types of immature, poorly crystalline minerals that have proven difficult to characterize (54, 55). More in-depth studies are required to obtain a precise understanding of the material properties and chemical characteristics unique to vascular calcific deposits, how BiP treatment alters the properties and morphology of microcalcifications, and how these changes influence the risk of plaque rupture. Our 3D collagen platform, amenable to high-resolution, multimodal analyses, has the potential to advance our understanding of the conditions and processes that drive the formation of plaque-destabilizing microcalcifications, as well as screen anticalcification drugs that aim to mitigate cardiovascular risk.

Materials and Methods

Cell Culture and Isolation of Extracellular Vesicles. Human coronary artery SMCs (PromoCell) were cultured for 14 d in either control "normal" medium of Dulbecco's Modified Eagle Medium (DMEM) plus 10% fetal bovine serum (FBS) and 1% penicillin/streptomycin, or calcifying "osteogenic" medium composed of control medium plus 10 nM dexamethasone, 100 μM L-ascorbic acid, and 10 mM β-glycerophosphate. The media were then exchanged for control or calcifying medium containing only 0.1% FBS, and after 24 h the

conditioned media was centrifuged and EV-containing supernatants were isolated. EV size distribution was quantified using nanoparticle tracking analysis (NTA), and calcification potential was assessed by measuring the activity of tissue non-specific alkaline phosphatase within the EV suspension, as detailed in *SI Appendix*.

EV-Nucleated Calcification in Collagen Hydrogels or in Suspension. Calcifying EVs were washed and concentrated using centrifugal filtration. The final vesicle suspension volume was adjusted to achieve a vesicle concentration four times that of the original vesicle concentration in conditioned media. The 3D collagen platform consisted of collagen hydrogels (5% type I collagen in 0.1% FBS calcifying medium) cast onto amino-silanated glass coverslips, as detailed in *SI Appendix*.

EVs were incubated for 8 d at 37 °C either with coverslip-adhered collagen hydrogels or in suspension. At the assigned time points, 0.4 mM ibandronate in water (Sigma-Aldrich) or an equivalent volume of water (untreated control) was added to the appropriate samples (final ibandronate concentration 0.05 mM). EV mineralization in suspension was quantified using a fluorescent-based mineral-binding dye (Lonza, OsteoImage), with results for Fig. 5*B* normalized using the average of the "no treatment" group for each biological replicate ($n = 5$ biological replicates).

Analysis of Calcifications Formed in 3D Collagen Platform. For SEM and EDS analysis, the coverslip-adhered hydrogels were fixed, dehydrated in grades of ethanol, subjected to critical point drying, mounted onto aluminum stubs, sputter coated with 5 nm of 80:20 platinum:palladium, and uncoated edges covered with silver adhesive. Samples were imaged in a Supra55VP FESEM (Zeiss) using a secondary electron in-lens detector and an EDS detector for elemental analysis. These protocols are further described in *SI Appendix*. An algorithm was custom-written (MATLAB) to calculate the average area of the five largest microcalcifications per high-powered field (2k magnification) imaged using SEM. Characteristics of individual microcalcifications (circularity and area) were measured using ImageJ. The MATLAB and ImageJ analyses are further detailed in *SI Appendix*.

For TEM, collagen hydrogels were prepared as above but cast in chambered coverglass wells. Calcifying EVs were concentrated 7.5× using centrifugal filtration (as above) and added to each gel. Following 8 d of incubation, samples were fixed and postfixed, dehydrated in grades of alcohol, infiltrated overnight in a 1:1 mixture of propyleneoxide and TAAB Epon, embedded in TAAB Epon, and polymerized. Ultrathin sections (~80 nm) were picked up onto copper grids stained with lead citrate and examined in a JEOL 1200EX transmission electron microscope. These protocols are further described in *SI Appendix*.

FTIR. For FTIR, vesicles were prepared and incubated in suspension as above, but the concentration of EVs used was 1× rather than 4×. Samples then underwent ultracentrifugation, and the pellet was dropcast onto an untreated glass slide. A motorized stage and polarized optical microscope were used to identify regions for analysis. Attenuated total reflectance mode (single bounce Ge crystal) was used to collect spectral data in a range from 4,000 to 600 cm^{-1}. Each spectrum was normalized to the sum of the values from 2,000 to 700 cm^{-1}. These protocols are further detailed in *SI Appendix*.

Confocal Microscopy. Confocal microscopy was used as a complementary imaging technique to visualize calcific deposits in the 3D hydrogels. Samples were stained using a near-infrared calcium tracer (OsteoSense 680, Perkin-Elmer), mounted on slides, and imaged by obtaining z-stack optical sections, each stack encompassing the entire fluorescent signal present within that region of the gel. The confocal microscopy protocol is further described in *SI Appendix*.

Multiscale FEA. A global finite element (FE) model and three fibrous cap submodels were prepared to obtain the SCF produced by the presence of a single microcalcification. For the global model, a 3D FE volumetric tetrahedral mesh was created, depicting the soft tissue, lipid, and cap of the atheroma. A total of 120 mmHg was applied as hydrostatic load on the lumen of the artery, and stresses and strains were recorded at each node. The 3D maps of stresses and strains were obtained for each SEM-imaged microcalcification. Control tests were performed by assigning soft tissue, hyperelastic properties to the 3D volume occupied by the microcalcifications. Stress concentration was calculated as the ratio of the stresses with and without microcalcifications
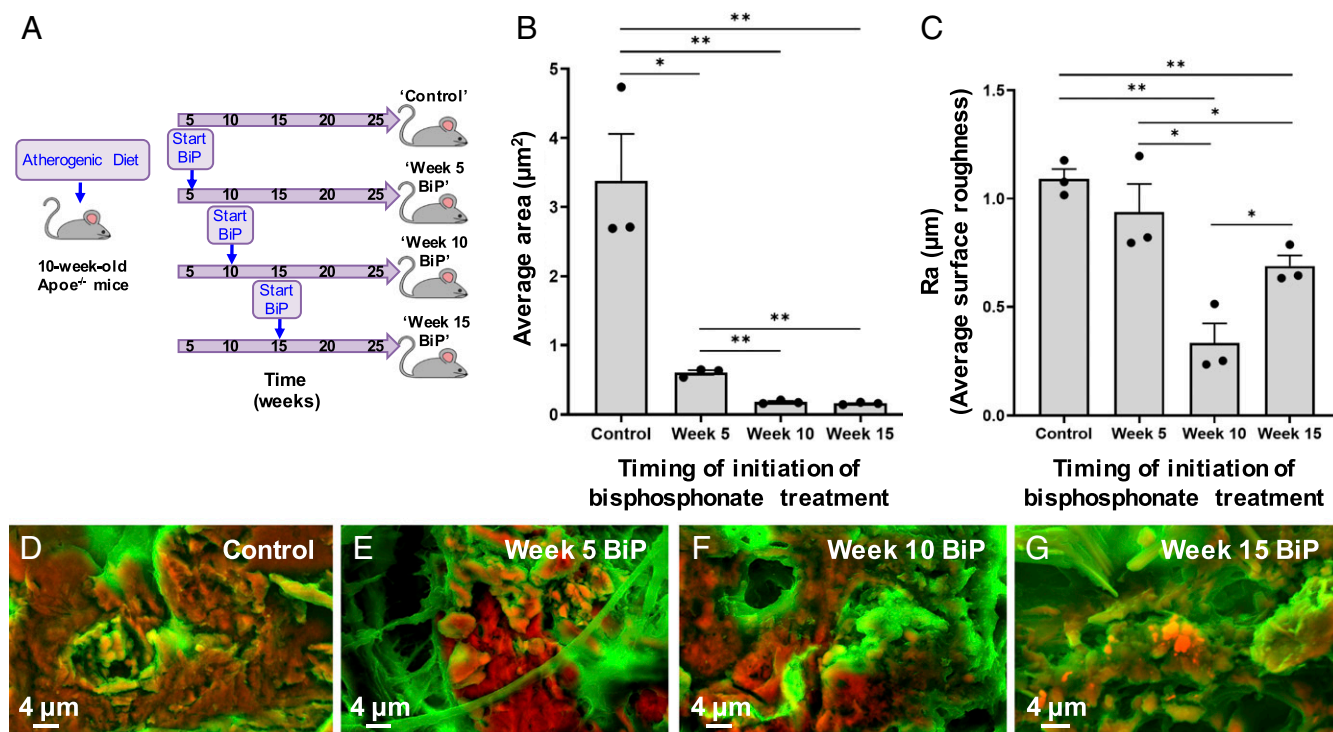
Ruiz et al.
Nanoanalytical analysis of bisphosphonate-driven alterations of microcalcifications using a
3D hydrogel system and in vivo mouse model

PNAS | 7 of 10
https://doi.org/10.1073/pnas.1811725118

Fig. 8. BiP treatment altered atherosclerotic plaque-associated calcification morphology in a time-dependent manner. ApoE$^{-/-}$ mice were fed an atherogenic diet and started on twice weekly BiP (ibandronate) treatment at various stages of atherosclerotic plaque development and calcification (*A*). Histological sections of aortic tissue were imaged using DDC-SEM. Quantitative image analysis was performed to measure the average area per individual calcification in each image (*B*) and the average surface roughness of calcific mineral in each image (*C*, $n = 3$ biological replicates per group; *$P < 0.05$, **$P < 0.01$, error bars represent SE of mean). Representative DDC-SEM images from each treatment group are shown (*D–G*).

and measured for five distinct microcalcifications per treatment group representing three biological replicates per group. A full description of the FEA process can be found in *SI Appendix*.

AFM. EVs were concentrated 4× and incubated in suspension and treated with ibandronate as above. Following 8 d of incubation, samples underwent ultracentrifugation, and the pellets were resuspended in MilliQ water with protease inhibitor 1:1,000, and spotted onto freshly cleaved mica sheets. Representative images were acquired with a NaioAFM (Nanosurf AG) equipped with Multi75Al-G probe in tapping mode. Imaging analysis was performed with the software WSxM 5.0 image (56). For detachment force measurements, samples were imaged using a NaioAFM (Nanosurf AG) equipped with ContAl-G probe (nominal spring constant k ~ 0.2 N·m^{-1}) in contact mode. The AFM probe was then positioned above the center of each EV/microcalcification, and individual force curves were recorded with a Z-starting offset of 500 nm and a Z-piezo speed of XYZ 10 μm·s^{-1}. Multiple EV/microcalcifications structures were probed in order to obtain a NDF value, representative of each sample. The software SPIP 6.7.2 (Image Metrology A/S) was then used to analyze the force-distance curves and obtain the detachment force values. These protocols are further described in *SI Appendix*.

Human Carotid Endarterectomy Tissue. Human carotid artery samples were obtained from patients undergoing endarterectomy, further described in *SI Appendix*. The image shown was generated using DDC-SEM, as detailed below.

Animal Study: Atherogenic Mouse Model Receiving Bisphosphonate Treatment. Eight-week-old mice homozygous for the Apoetm1Unc mutation (B6.129P2-Apoetm1Unc/J, ApoE$^{-/-}$) were purchased from The Jackson Laboratory, with a mortality rate for this experiment of <9% as expected in the setting of some challenges with animal handling unrelated to the experimental design. After 2 wk of incubation and feeding with chow diet, $n = 16$ animals (10 wk old) received an atherogenic diet (ENVIGO, TD.88137 adjusted calories diet, 42% from fat) for 25 wk. The animals were sorted into four groups,

$n = 4$ animals per group. There was no significant difference among endpoint animal body weight among the mice in each group (*SI Appendix*, Fig. S10). Three groups received twice weekly subcutaneous injections of bisphosphonate ibandronate sodium (2 mg/kg mouse per dose, APEXBIO) after 5, 10, and 15 wk of diet, respectively, further detailed in *SI Appendix*. After 25 wk, the mice were killed, and the aortas were resected, fixed, and embedded, cut into 18-μm thick histological sections (further detailed in *SI Appendix*), and prepared for SEM, detailed below. Histology was also performed including H&E and Alizarin Red S staining, as detailed in *SI Appendix*.

Density-Dependent Color SEM. Histological sectioned samples were secured to an aluminum sample holder with carbon tape, and silver paint was applied to the area immediately surrounding each sample, which was then coated with carbon. Following the coating procedure, samples were imaged by an SEM (Carl Zeiss EVO 25 SEM) operated at 15 kV (mouse tissue samples) or 10 kV (human tissue sample). The secondary electron (SE) and backscattered electron (BSE) detectors were used to image the same region of the samples. To obtain DDC-SEM (37), using ImageJ software, both images were stacked and the SE image was assigned to the green channel, whereas the BSE image was assigned to the red channel.

Quantitative Analysis of In Vivo Calcification Size and Roughness. To assess the average of the mineral surface roughness (Ra) and the average area of microcalcifications imaged from histologic samples via DDC-SEM, a custom image analysis script was developed in MATLAB, based on previous methods of quantifying roughness by analyzing deviations in grayscale intensity (57–59), further described in *SI Appendix*. The Ra and area values were averaged across images for each mouse, and the data reported represent the mean values calculated from different mice, n = 3 biological replicates.

Statistical Analyses. Error bars represent SD unless stated otherwise. Quantitative data were analyzed for statistical significance using a Student's *t* test

Ruiz et al.
Nanoanalytical analysis of bisphosphonate-driven alterations of microcalcifications using
a 3D hydrogel system and in vivo mouse model

(Microsoft Excel) if comparing two groups, or a one-way ANOVA (Graph-Pad Prism) if comparing multiple groups, further detailed in *SI Appendix*. For *SI Appendix*, Figs. S5 and S6, a two-way comparison between multiple variables was performed using a two-way ANOVA or mixed effects model, respectively (*SI Appendix,* Figs. S5 and S6). Significance was defined as $P < 0.05$.

The statistics for *SI Appendix*, Fig. S7 are an exception, as detailed in *SI Appendix*. The error bars represent a normalized error value, accounting for error propagation using classical error theory.

Data Availability. All study data are included in the article and/or supporting information.

1. D. Lloyd-Jones *et al.*; American Heart Association Statistics Committee and Stroke Statistics Subcommittee, Executive summary: Heart disease and stroke statistics–2010 update: A report from the American heart association. *Circulation* **121**, 948–954 (2010).

2. A. S. Go *et al.*; American Heart Association Statistics Committee and Stroke Statistics Subcommittee, Executive summary: Heart disease and stroke statistics–2013 update: A report from the American heart association. *Circulation* **127**, 143–152 (2013).

3. R. Vliegenthart *et al.*, Coronary calcification improves cardiovascular risk prediction in the elderly. *Circulation* **112**, 572–577 (2005).

4. S. S. Martin *et al.*, Dyslipidemia, coronary artery calcium, and incident atherosclerotic cardiovascular disease: Implications for statin therapy from the multi-ethnic study of atherosclerosis. *Circulation* **129**, 77–86 (2014).

5. M. Ferencik *et al.*, A computed tomography-based coronary lesion score to predict acute coronary syndrome among patients with acute chest pain and significant coronary stenosis on coronary computed tomographic angiogram. *Am. J. Cardiol.* **110**, 183–189 (2012).

6. S. Ehara *et al.*, Spotty calcification typifies the culprit plaque in patients with acute myocardial infarction: An intravascular ultrasound study. *Circulation* **110**, 3424–3429 (2004).

7. M. H. Criqui *et al.*, Calcium density of coronary artery plaque and risk of incident cardiovascular events. *JAMA* **311**, 271–278 (2014).

8. K. K. Wong, P. Thavornpattanapong, S. C. Cheung, Z. Sun, J. Tu, Effect of calcification on the mechanical stability of plaque based on a three-dimensional carotid bifurcation model. *BMC Cardiovasc. Disord.* **12**, 7 (2012).

9. A. Kelly-Arnold *et al.*, Revised microcalcification hypothesis for fibrous cap rupture in human coronary arteries. *Proc. Natl. Acad. Sci. U.S.A.* **110**, 10741–10746 (2013).

10. N. Maldonado, A. Kelly-Arnold, L. Cardoso, S. Weinbaum, The explosive growth of small voids in vulnerable cap rupture; cavitation and interfacial debonding. *J. Biomech.* **46**, 396–401 (2013).

11. J. L. Ruiz, S. Weinbaum, E. Aikawa, J. D. Hutcheson, Zooming in on the genesis of atherosclerotic plaque microcalcifications. *J. Physiol.* **594**, 2915–2927 (2016).

12. Y. Vengrenyuk *et al.*, A hypothesis for vulnerable plaque rupture due to stress-induced debonding around cellular microcalcifications in thin fibrous caps. *Proc. Natl. Acad. Sci. U.S.A.* **103**, 14678–14683 (2006).

13. K. M. Kim, Calcification of matrix vesicles in human aortic valve and aortic media. *Fed. Proc.* **35**, 156–162 (1976).

14. A. Tanimura, D. H. McGregor, H. C. Anderson, Matrix vesicles in atherosclerotic calcification. *Proc. Soc. Exp. Biol. Med.* **172**, 173–177 (1983).

15. H. H. Hsu, N. P. Camacho, Isolation of calcifiable vesicles from human atherosclerotic aortas. *Atherosclerosis* **143**, 353–362 (1999).

16. A. L. Durham, M. Y. Speer, M. Scatena, C. M. Giachelli, C. M. Shanahan, Role of smooth muscle cells in vascular calcification: Implications in atherosclerosis and arterial stiffness. *Cardiovasc. Res.* **114**, 590–600 (2018).

17. Y. Tintut, J. Patel, F. Parhami, L. L. Demer, Tumor necrosis factor-α promotes in vitro calcification of vascular cells via the cAMP pathway. *Circulation* **102**, 2636–2642 (2000).

18. E. Aikawa *et al.*, Osteogenesis associates with inflammation in early-stage atherosclerosis evaluated by molecular imaging in vivo. *Circulation* **116**, 2841–2850 (2007).

19. L. L. Demer, Y. Tintut, Vascular calcification: Pathobiology of a multifaceted disease. *Circulation* **117**, 2938–2948 (2008).

20. S. E. New *et al.*, Macrophage-derived matrix vesicles: An alternative novel mechanism for microcalcification in Atherosclerotic Plaques. *Circ. Res.* **113**, 72–77 (2013).

21. R. Kawakami *et al.*, S100A9-RAGE Axis Accelerates formation of macrophage-mediated extracellular vesicle microcalcification in diabetes mellitus. *Arterioscler. Thromb. Vasc. Biol.* **40**, 1838–1853 (2020).

22. C. M. Stanford, P. A. Jacobson, E. D. Eanes, L. A. Lembke, R. J. Midura, Rapidly forming apatitic mineral in an osteoblastic cell line (UMR 106-01 BSP). *J. Biol. Chem.* **270**, 9420–9428 (1995).

23. K. Drabek, J. van de Peppel, M. Eijken, J. P. van Leeuwen, GPM6B regulates osteoblast function and induction of mineralization by controlling cytoskeleton and matrix vesicle release. *J. Bone Miner. Res.* **26**, 2045–2051 (2011).

24. J. D. Hutcheson *et al.*, Genesis and growth of extracellular-vesicle-derived microcalcification in atherosclerotic plaques. *Nat. Mater.* **15**, 335–343 (2016).

25. H. C. Anderson, Matrix vesicles and calcification. *Curr. Rheumatol. Rep.* **5**, 222–226 (2003).

26. A. N. Kapustin *et al.*, Calcium regulates key components of vascular smooth muscle cell-derived matrix vesicles to enhance mineralization. *Circ. Res.* **109**, e1–e12 (2011).

27. A. Tanimura, D. H. McGregor, H. C. Anderson, Calcification in atherosclerosis. I. Human studies. *J. Exp. Pathol.* **2**, 261–273 (1986).

28. M. A. Rogers *et al.*, Annexin A1-dependent tethering promotes extracellular vesicle aggregation revealed with single-extracellular vesicle analysis. *Sci. Adv.* **6**, eabb1244 (2020).

29. H. Fleisch, Bisphosphonates: Mechanisms of action. *Endocr. Rev.* **19**, 80–100 (1998).

30. D. A. Prosdocimo, D. C. Douglas, A. M. Romani, W. C. O'Neill, G. R. Dubyak, Autocrine ATP release coupled to extracellular pyrophosphate accumulation in vascular smooth muscle cells. *Am. J. Physiol. Cell Physiol.* **296**, C828–C839 (2009).

31. M. T. Drake, B. L. Clarke, E. M. Lewiecki, The pathophysiology and treatment of osteoporosis. *Clin. Ther.* **37**, 1837–1850 (2015).

32. P. A. Price, S. A. Faus, M. K. Williamson, Bisphosphonates alendronate and ibandronate inhibit artery calcification at doses comparable to those that inhibit bone resorption. *Arterioscler. Thromb. Vasc. Biol.* **21**, 817–824 (2001).

33. K. A. Lomashvili, M.-C. Monier-Faugere, X. Wang, H. H. Malluche, W. C. O'Neill, Effect of bisphosphonates on vascular calcification and bone metabolism in experimental renal failure. *Kidney Int.* **75**, 617–625 (2009).

34. J. E. Hartle *et al.*, Bisphosphonate therapy, death, and cardiovascular events among female patients with CKD: A retrospective cohort study. *Am. J. Kidney Dis.* **59**, 636–644 (2012).

35. R. M. Perkins *et al.*, Bisphosphonates and mortality in women with CKD and the presence or absence of cardiovascular disease. *Clin. J. Am. Soc. Nephrol.* **9**, 874–880 (2014).

36. S. Elmariah *et al.*, Bisphosphonate use and prevalence of valvular and vascular calcification in women MESA (the multi-ethnic study of atherosclerosis). *J. Am. Coll. Cardiol.* **56**, 1752–1759 (2010).

37. S. Bertazzo *et al.*, Nano-analytical electron microscopy reveals fundamental insights into human cardiovascular tissue calcification. *Nat. Mater.* **12**, 576–583 (2013).

38. C. Thouverey, G. Bechkoff, S. Pikula, R. Buchet, Inorganic pyrophosphate as a regulator of hydroxyapatite or calcium pyrophosphate dihydrate mineral deposition by matrix vesicles. *Osteoarthritis Cartilage* **17**, 64–72 (2009).

39. N. Pleshko, A. Boskey, R. Mendelsohn, Novel infrared spectroscopic method for the determination of crystallinity of hydroxyapatite minerals. *Biophys. J.* **60**, 786–793 (1991).

40. P. Kalia *et al.*, Nanohydroxyapatite shape and its potential role in bone formation: An analytical study. *J. R. Soc. Interface* **11**, 20140004 (2014).

41. S.-Y. Lin, T.-K. Wu, H.-J. Chiou, T. H.-S. Hsu, C.-C. Lin, Infrared microspectroscopic imaging as a probing tool to fast distinguish chemical compositions in calcified deposits of prostatic calculi and calcific tendonitis. *Spectroscopy (Springf.)* **25**, 207–216 (2011).

42. R. Garimella, X. Bi, H. C. Anderson, N. P. Camacho, Nature of phosphate substrate as a major determinant of mineral type formed in matrix vesicle-mediated in vitro mineralization: An FTIR imaging study. *Bone* **38**, 811–817 (2006).

43. S. J. Gadaleta, E. P. Paschalis, F. Betts, R. Mendelsohn, A. L. Boskey, Fourier transform infrared spectroscopy of the solution-mediated conversion of amorphous calcium phosphate to hydroxyapatite: New correlations between X-ray diffraction and infrared data. *Calcif. Tissue Int.* **58**, 9–16 (1996).

44. G. R. Sauer, R. E. Wuthier, Fourier transform infrared characterization of mineral phases formed during induction of mineralization by collagenase-released matrix vesicles in vitro. *J. Biol. Chem.* **263**, 13718–13724 (1988).

45. C. Rey *et al.*, Nanocrystalline apatites in biological systems: Characterisation, structure and properties. *Materialwiss. Werkstofftech.* **38**, 996–1002 (2007).

46. S. J. Gadaleta, E. P. Paschalis, F. Betts, R. Mendelsohn, A. L. Boskey, Fourier transform infrared spectroscopy of the solution-mediated conversion of amorphous calcium phosphate to hydroxyapatite : New correlations between x-ray diffraction and infrared data. *Calcif. Tissue Int.* **58**, 9–16 (1996).

Ruiz et al.
Nanoanalytical analysis of bisphosphonate-driven alterations of microcalcifications using a 3D hydrogel system and in vivo mouse model

PNAS | 9 of 10
https://doi.org/10.1073/pnas.1811725118

47. C. Goettsch *et al.*, Sortilin mediates vascular calcification via its recruitment into extracellular vesicles. *J. Clin. Invest.* **126**, 1323–1336 (2016).

48. M. Derwall *et al.*, Inhibition of bone morphogenetic protein signaling reduces vascular calcification and atherosclerosis. *Arterioscler. Thromb. Vasc. Biol.* **32**, 613–622 (2012).

49. Y. Yao *et al.*, Inhibition of bone morphogenetic proteins protects against atherosclerosis and vascular calcification. *Circ. Res.* **107**, 485–494 (2010).

50. R. G. G. Russell, N. B. Watts, F. H. Ebetino, M. J. Rogers, Mechanisms of action of bisphosphonates: Similarities and differences and their potential influence on clinical efficacy. *Osteoporos. Int.* **19**, 733–759 (2008).

51. F. Errassifi *et al.*, Infrared, Raman and NMR investigations of risedronate adsorption on nanocrystalline apatites. *J. Colloid Interface Sci.* **420**, 101–111 (2014).

52. L. Cardoso, A. Kelly-Arnold, N. Maldonado, D. Laudier, S. Weinbaum, Effect of tissue properties, shape and orientation of microcalcifications on vulnerable cap stability using different hyperelastic constitutive models. *J. Biomech.* **47**, 870–877 (2014).

53. N. X. Chen, K. D. O'Neill, X. Chen, S. M. Moe, Annexin-mediated matrix vesicle calcification in vascular smooth muscle cells. *J. Bone Miner. Res.* **23**, 1798–1805 (2008).

54. S. V. Dorozhkin, Calcium orthophosphates. *J. Mater. Sci.* **42**, 1061–1095 (2007).

55. J. C. Elliott, Calcium phosphate biominerals. *Rev. Mineral. Geochem.* **48**, 427–453 (2002).

56. I. Horcas *et al.*, WSXM: A software for scanning probe microscopy and a tool for nanotechnology. *Rev. Sci. Instrum.* **78**, 013705 (2007).

57. G. Samtaş, Measurement and evaluation of surface roughness based on optic system using image processing and artificial neural network. *Int. J. Adv. Manuf. Technol.* **73**, 353–364 (2014).

58. R. Kamguem, S. A. Tahan, V. Songmene, Evaluation of machined part surface roughness using image texture gradient factor. *Int. J. Precis. Eng. Manuf.* **14**, 183–190 (2013).

59. K. A. Alshibli, A. M. Druckrey, R. I. Al-Raoush, T. Weiskittel, N. V. Lavrik, Quantifying morphology of sands using 3D imaging. *J. Mater. Civ. Eng.* **27**, 04014275 (2015).

10 of 10 | **PNAS**
https://doi.org/10.1073/pnas.1811725118

Ruiz et al.
Nanoanalytical analysis of bisphosphonate-driven alterations of microcalcifications using a 3D hydrogel system and in vivo mouse model